








## Structural modulation driven Curie temperature enhancement in Cr-doped SrRuO<sub>3</sub>

Pooja <sup>1,\*</sup>, Bikash Saha <sup>2</sup>, Nitesh Choudhary <sup>3</sup>, Pradip K. Maji <sup>3</sup>, A. K. Bera <sup>2,4</sup>, S. M. Yusuf <sup>2,4</sup> and Chanchal Sow <sup>1,†</sup>

<sup>1</sup>Department of Physics, Indian Institute of Technology Kanpur, Kanpur 208016, India

<sup>2</sup>Solid State Physics Division, Bhabha Atomic Research Centre, Mumbai 400085, India

<sup>3</sup>Department of Polymer and Process Engineering, Indian Institute of Technology Roorkee, Saharanpur Campus 247001, U.P., India

<sup>4</sup>Homi Bhabha National Institute, Anushaktinagar, Mumbai 400094, India



(Received 6 December 2023; revised 24 February 2024; accepted 29 February 2024; published 3 April 2024; corrected 12 April 2024)

A strongly correlated system with competing ground states is often poised close to the quantum critical point. External perturbations such as pressure, strain, electric field, and chemical doping can stabilize its ground state with exotic physical properties. Cr-doping is the lone exception, which enhances the Curie temperature in one such correlated system, SrRuO<sub>3</sub>. To find the origin of  $T_C$  enhancement, we investigate the temperature-dependent structure, spectroscopic, magnetic, and magnetotransport properties in SrRu<sub>1-x</sub>Cr<sub>x</sub>O<sub>3</sub>. Cr-doping squeezes the unit cell volume, which effectively enhances the stretching octahedral distortion nearly five times more than pure SrRuO<sub>3</sub>. The Curie temperature increment of  $\sim 22$  K for  $x = 0.15$  is found to be intertwined with the structural modulation. Temperature-dependent neutron diffraction analysis indicates that the unit cell volume minima coincide exactly with the enhanced ferromagnetic ordering ( $\sim 190$  K). Further analysis reveals that the effect of Cr-doping not only freezes the octahedral tilt below 100 K but also suppresses the complex magnetism responsible for exchange bias and the topological Hall effect in SrRuO<sub>3</sub>. The spectroscopic measurements find a reduction of itinerancy of  $d$ -electrons with Cr-doping. The magnetotransport measurements portray an evolution from itinerant to localized ferromagnetism.

DOI: [10.1103/PhysRevB.109.144404](https://doi.org/10.1103/PhysRevB.109.144404)

### I. INTRODUCTION

Quantum materials with tunable multifunctionalities are an attractive area of research due to their intriguing magnetic, electronic, and optical characteristics [1–3]. Such diverse physical properties bring vast possibilities for applications in microelectronic, magnetic, and spintronic devices [4]. Tuning the relative strength of spin-orbit coupling ( $\lambda$ ) and on-site Coulomb interaction ( $U$ ) from low to high, various quantum phases have emerged [5]. In particular, ruthenates with moderate strength of  $\lambda/U$  become interesting candidates as they lie near the crossover region. The layered ruthenates, especially in the Ruddlesden-Popper (RP) series (Sr/Ca)<sub>1+n</sub>Ru<sub>n</sub>O<sub>3n+1</sub>, where  $n$  ( $1 \leq n \leq \infty$ ) is the number of Ru-O layers, exhibit a drastic change of physical properties with a change in  $n$ . In the Ca-based RP series, a robust antiferromagnetic (AFM) insulating state (Mott insulator [6]) is stabilized for  $n = 1$ , which gradually decreases with increasing  $n$ . Thus the magnetic state of metallic CaRuO<sub>3</sub> (end member) is critically poised among AFM, ferromagnetic (FM), and paramagnetic (PM) [7,8]. Sr<sub>2</sub>RuO<sub>4</sub> ( $n = 1$ ) is a nonmagnetic metal down to 2 K and becomes a  $p$ -type superconductor below 1.5 K [9]. For  $n > 2$ , the ferromagnetic metallic state is stabilized in Sr-based RP series, and the Curie temperature is enhanced with  $n$ . The end member SrRuO<sub>3</sub> ( $n = \infty$ ) is an itinerant ferromagnet below  $T_C \sim 166$  K [7]. SrRuO<sub>3</sub> identifies

with distorted orthorhombic ( $Pnma$ ) perovskite structure with sizable  $U$  ( $=3-3.5$  eV [10]) and  $\lambda$  ( $=40-80$  meV [11]). In addition, SrRuO<sub>3</sub> also possesses strong hybridization between Ru- $4d$  and O- $2p$  orbitals. These features facilitate a diverse range of intriguing physical characteristics in SrRuO<sub>3</sub> [12–16]. The recent finding of the topological Hall effect and magnetic skyrmions in SrRuO<sub>3</sub> thin films arising due to interfacial strain has attracted considerable interest [17–20].

In bulk systems, external perturbations such as pressure, temperature, internal strain by chemical doping, and electric field change the physical properties drastically. For example, the crystal structure undergoes perovskite ( $Pbnm$ ) to post-perovskite ( $Cmcm$ ) structure accompanied by a 1.9% volume collapse with the application of high pressure ( $\sim 40$  GPa) [21], which also alters the magnetism by decreasing the Ru-O bond lengths [22]. On the other hand, temperature also drives two structural phase transitions from orthorhombic to tetragonal (at 800 K) and from tetragonal to cubic (at 975 K) [23]. Chemical doping provides an additional method for tuning the magnetic exchange by internally deforming the structure. The size of the cation can be chosen higher or lower than Ru depending on the requirement of unit cell volume expansion or contraction [24]. This also affects the orthorhombicity and distortion in RuO<sub>6</sub> octahedra, thereby a significant change in the magnetism [25–27]. In particular, SrRu<sub>1-x</sub>M<sub>x</sub>O<sub>3</sub>, where  $M$  ( $=Zn^{2+}$ ,  $Mn^{3+}$ ,  $Co^{2+}$ ,  $Ni^{2+}$ , and  $Ti^{4+}$ ) is a transition-metal ion (TMI) that suppresses the  $T_C$  down to 100 K [28,29]. Doping Cr is an exceptional case (among TMIs) that enhances the  $T_C$  of SrRuO<sub>3</sub> up to  $\sim 190$  K [30,31]. The enhancement of  $T_C$  ( $\sim 210$  K) is also noticed in Pb-doped SrRuO<sub>3</sub>, and

\*kpooja@iitk.ac.in

†chanchal@iitk.ac.in

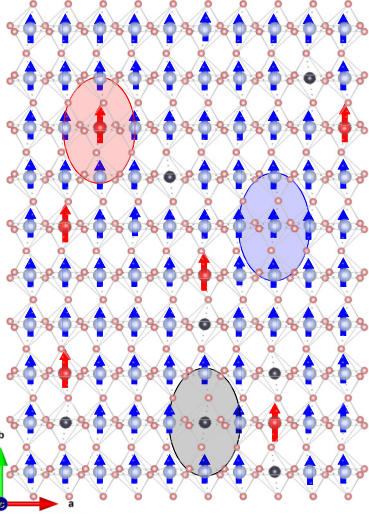


FIG. 1. Schematic representation of a  $10 \times 10 \times 1$  cell of  $\text{SrRu}_{1-x}\text{Cr}_x\text{O}_3$ . Here only the Ru (light blue balls) and oxygen (light red balls) atoms are shown for clarity. The Cr atoms (shown in red and black balls) are randomly distributed in the Ru matrix. The magnetic moments of  $\text{Ru}^{4+}$  ( $S = 1$ ) and  $\text{Cr}^{3+}$  ( $S = 3/2$ ) are shown with blue and red arrows, respectively, and they are ferromagnetically aligned along the  $b$ -axis.  $\text{Cr}^{6+}$  ( $S = 0$ ) are shown as black balls that are nonmagnetic and act as a disorder. In such a system, there are two dominant exchanges: the blue circled region has pure Ru-Ru FM exchange, and the red region has Ru-Cr FM exchange. The gray region (which contains the nonmagnetic Cr) is mainly involved in reducing the range of exchange interaction, whereas the red region enhances the strength of the exchange interaction more than SRO.

the origin is found to be structural distortion [31]. However, the origin of increased  $T_C$  with Cr-doping in  $\text{SrRuO}_3$  is still not clear. A schematic picture of magnetic moments with possible exchange interactions in  $\text{SrRu}_{1-x}\text{Cr}_x\text{O}_3$  is depicted in Fig. 1. Experimental reports suggest the mixed valence state of ruthenium, which creates  $\text{Ru}^{4+/5+}-\text{O}-\text{Cr}^{4+/3+}$  minority double exchange interaction and enhances the ordering temperature [30,32,33], while the first-principles calculation (using LSDA, LSDA+U, and GGA+U) explains the origin of the increased  $T_C$  in the  $\text{SrRu}_{1-x}\text{Cr}_x\text{O}_3$  system in terms of  $\text{Cr}^{4+} - \text{Ru}^{4+}$  hybridization [34] and  $p$ - $d$  coupling [35].

To find a clear picture of such  $T_C$  enhancement, we present a detailed and systematic structural, spectroscopic, magnetic, transport, and microscopic magnetic state by neutron diffraction studies on single-phase  $\text{SrRu}_{1-x}\text{Cr}_x\text{O}_3$  ( $0 \leq x \leq 0.15$ ) samples. Our study established a strong connection between structural modulation with the increased  $T_C$  in Cr-doped  $\text{SrRuO}_3$ .

## II. SAMPLE PREPARATION AND EXPERIMENTAL DETAILS

High-quality  $\text{SrRu}_{1-x}\text{Cr}_x\text{O}_3$  ( $0 \leq x \leq 0.15$ ) (SRCO) samples are synthesized via the solid-state reaction method. Powders of  $\text{SrCO}_3$  (>99.95%),  $\text{RuO}_2$  (>99.9%), and  $\text{Cr}_2\text{O}_3$  (>99.9%) are used as ingredients. The mixture is pelletized and sintered for 48 h at 900–1400 °C with multiple intermediate grindings.  $\text{RuO}_2$  is volatile as it sublimates at 1200 °C. To compensate, the extra 5 wt.% of  $\text{RuO}_2$  is added to preserve the

TABLE I. EPMA results: Atomic percentage of Ru% and Cr% with the nominal ( $x_{\text{nom}}$ ) and determined ( $x_{\text{det}}$ ) value of  $x$  in  $\text{SrRu}_{1-x}\text{Cr}_x\text{O}_3$  samples.

Sample	$x_{\text{nom}}$	$x_{\text{det}}$	Ru%	Cr%
SRO	0	0	102.0	0
SRCO5	0.05	0.07	87.9	7.06
SRCO10	0.10	0.11	90.32	11.51
SRCO15	0.15	0.15	86.52	15.86

stoichiometric ratio. The atomic percentage of Ru and Cr is examined by the electron probe microscopy analyzer (EPMA) equipped with JXA-8230, and JEOL (as tabulated in Table I). The phase purity and crystallinity of all samples are checked by using a high-resolution x-ray powder diffractometer (PAN analytical Empyrean  $\text{Cu } K\alpha$ ). The valence states of Cr, Ru, and Sr are verified by PHI Versa Probe-II x-ray photoelectron spectroscopy (XPS) consisting of a monochromatic Al  $K\alpha$  ( $h\nu = 1486.6$  eV) source. The magnetic and transport measurements are conducted between 2–300 K temperature and 0–6 T of applied magnetic field range using commercial quantum design MPMS (MPMS-XL) and PPMS, respectively. Temperature-dependent (5–300 K) Neutron diffraction (ND) measurements are carried out on a high-quality SRCO15 polycrystalline sample using a powder neutron diffractometer, PD-I, at Dhruva Research Reactor, Mumbai (India). The powder sample is filled in a cylindrical vanadium can and attached to the cold finger of the He-4 gas-based closed-cycle refrigerator.

## III. CALCULATION DETAILS

The spin-polarized density of states (DOSs) calculation is carried out on  $\text{SrRuO}_3$  by using the generalized gradient approximation (GGA) and the GGA+U method with QUANTUM ESPRESSO [36]. The Hubbard U term, which is the Coulomb repulsion between on-site electrons, is considered to understand the effect of electron correlation on DOSs. We considered the conventional cell ( $Z = 4$ ) of  $\text{SrRuO}_3$  consisting of 20 atoms with lattice parameters obtained from Rietveld-refined XRD-data for SRO and SRCO15 (without any structural relaxation calculation). The calculation is performed with  $4 \times 4 \times 4$   $K$ -points by using the Perdew-Burke-Ernzerhof (PBE) exchange-correlation functional [37]. The ultrasoft pseudopotentials (USPPs), and a basis set for valence electrons consisting of plane waves with a cutoff energy of 25 Rydberg (340 eV), are used for self-consistent calculation. To understand the electron correlation effect on the DOS, the value of  $U$  is taken as 3.5 eV [35] for an Ru atom.

## IV. RESULTS AND DISCUSSION

### A. Structural analysis

Figures 2(a) and 2(b) display the experimentally measured and calculated Rietveld-refined (using FULLPROF [39]) x-ray diffraction patterns of the SRO and SRCO15, respectively. Rietveld analysis reveals that SRCO samples have an orthorhombic crystal symmetry ( $a \neq b \neq c, \alpha = \beta = \gamma = 90$ ) with space group  $Pnma$  (62) [32,40]. The Cr atom occupies

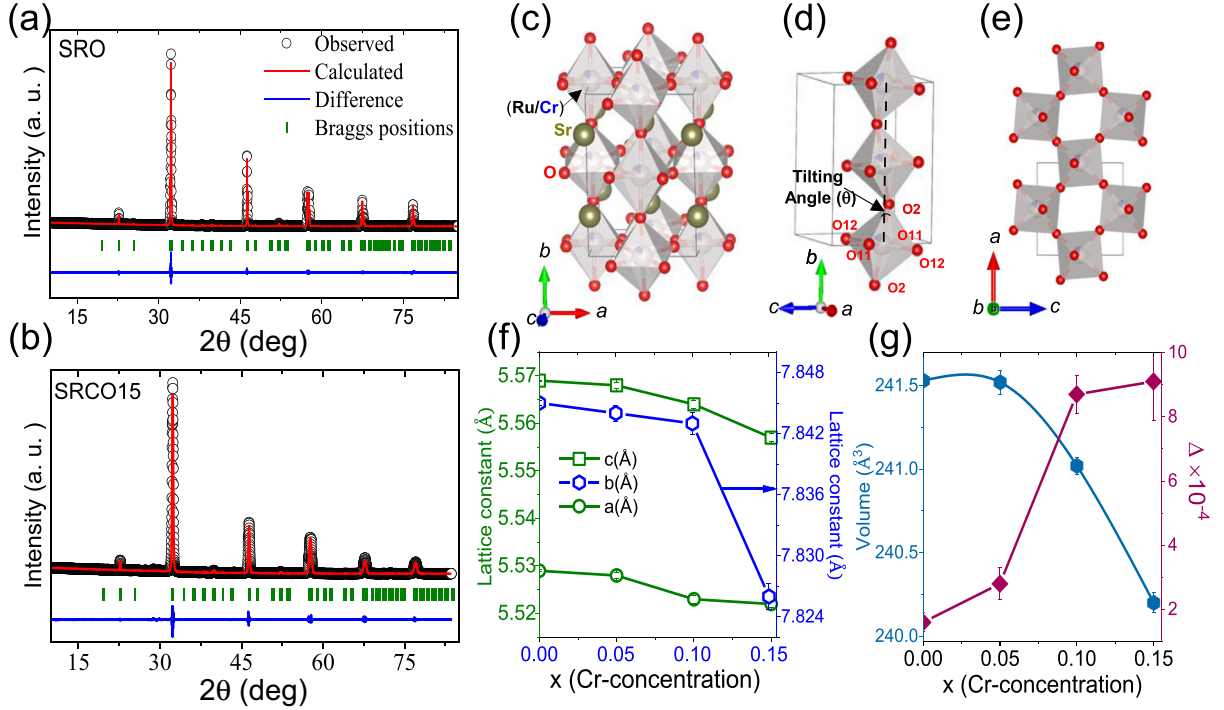


FIG. 2. Rietveld refined x-ray diffraction pattern of (a) SRO and (b) SRCO15. The open black circles and red solid lines are observed and calculated patterns, respectively, and the blue line shows the difference between observed and calculated patterns, whereas green vertical bars are allowed Bragg peak positions. (c) The orthorhombic crystal structure of SRCO15 along with (Ru/Cr) $O_6$  octahedral arrangement. The crystal structure is drawn using VESTA visualizing program [38], from the output file after Rietveld refinements. Schematics of (Ru/Cr) $O_6$  octahedra to demonstrate the octahedral tilt and various oxygen atoms in the (d)  $bc$ -plane and (e)  $ac$ -plane. The black solid line represents the unit cell. Variation of (f) lattice constants, (g) unit cell volume (left y-axis), and  $\Delta$  (right-y axis) is shown upon Cr doping.

the same Wyckoff-4a site as the Ru atom. The schematic crystal structure is shown in Fig. 2(c). The crystal structure consists of corner-sharing identical (Ru/Cr) $O_6$  octahedra with tilt along all three directions, as shown in Figs. 2(d) and 2(e). Figure 2(f) shows the variation of lattice constant with respect to Cr-content. At 15% Cr-doping the lattice constants  $a$ ,  $b$ , and  $c$  decrease by  $\sim 0.13\%$ ,  $0.24\%$ , and  $0.22\%$ , respectively. As a result, the overall  $\sim 0.54\%$  decrease in unit cell volume is shown in Fig. 2(g). The decrease in the unit cell volume is attributed to the smaller cationic radius of  $Cr^{6+}$  (0.044 nm) or  $Cr^{3+}$  (0.061 nm) (confirmed by XPS) compared to  $Ru^{4+}$  (0.062 nm). The refined crystal structure reveals three distinct octahedral bond lengths, namely Ru-O11 (basal), Ru-O12 (basal), and Ru-O2 (apical) with values 1.976, 2.0596, and 1.929 Å, respectively, in the case of SRCO15. The unequal bond lengths give rise to the octahedral distortion [41]. The octahedral stretching distortions ( $\Delta$ ) and angular distortions ( $\Sigma$ ) can be calculated using the equations

$$\Delta = \frac{1}{6} \sum_{i=1}^6 \left[ \frac{|d_i - d_{\text{mean}}|}{d_{\text{mean}}} \right]^2, \quad (1)$$

$$\Sigma = \frac{1}{12} \sum_{i=1}^{12} |\phi_i - 90|, \quad (2)$$

respectively, where  $d_{\text{mean}}$  and  $d_i$  denote the average and  $i$ th Ru/Cr-O bond length (there are a total of six different Ru-O lengths in a  $RuO_6$  octahedra), respectively. The angle  $\phi_i$  is considered as  $i$ th O-(Ru/Cr)-O bond angles in the (Ru/Cr) $O_6$  octahedra. The stretching distortion increases as we increase

the Cr-doping in SRO. At 15% Cr-doping, the value of  $\Sigma$  is increased by 22%, whereas  $\Delta$  is enhanced by nearly five times compared to parent compound SRO. Such increased distortion due to Cr-doping affects the superexchange/double-exchange interaction between Ru moments. In this regard, theoretical work by Wang *et al.* suggests that for low Cr-doped samples ( $x < 0.25$ ),  $Cr^{3+}$  couples ferromagnetically with  $Ru^{4+}$  moments, which is responsible for enhancement of the  $T_C$  [35]. The calculated value of  $\Sigma$ ,  $\Delta$ , and derived lattice parameters of SRCO15 in comparison with SRO at room temperature are tabulated in Table II.

## B. X-ray photoelectrons spectroscopy

X-ray photoelectron spectroscopy (XPS) is employed to investigate the valence states of various constituent elements and the density of states (DOSs) in the vicinity of Fermi energy ( $E_F$ ). The XPS survey scan identifies the presence of Sr, Ru, Cr, and O in SRCO samples (not shown here). Figure 3(a) depicts the Ru 3d XPS core spectra of SRO and SRCO15 (the intensity is normalized by removing the Shirley background after fitting). The peak at  $\sim 278$  eV is agreed to be  $Sr3p_{1/2}$  and the other two peaks in the Ru 3d spectra correspond to a spin-orbit doublet (SOD): Ru  $3d_{5/2}$  and Ru  $3d_{3/2}$  with splitting energy  $\Delta E_{SO}^{Ru} \sim 5$  eV, suggesting a  $Ru^{4+}$  valence state [42] in all samples. Each Ru doublet has two peaks labeled screened ( $s$ ) and unscreened ( $u$ ). The  $s$  peak is generally present at  $\sim 2$  eV lower binding energy (B.E.) than the  $u$  peak in metallic systems due to the screening



TABLE II. Rietveld-refinement structural parameters of SRO and SRCO15 in comparison with the room-temperature ND results.

Sample	$a$ (Å)	$b$ (Å)	$c$ (Å)	$V$ (Å <sup>3</sup> )	Ru-O1-Ru (deg)	Ru-O2-Ru (deg)	$\Sigma$	$\Delta$
SRO	5.529	7.845	5.569	241.5	163.9	159.1	4.5	$1.6 \times 10^{-4}$
SRCO15	5.522	7.826	5.557	240.2	163.5	157.9	5.5	$9.1 \times 10^{-4}$

effect of core electrons [43]. The presence of both peaks also indicates that the samples are metallic at room temperature. It is important to note that in the case of SRCO15, the Ru core spectra are shifted towards higher binding energy. The shift is visible in the zoomed-in view of the Ru  $3d_{5/2}$  peak in the inset of Fig. 3(a). This spectral shift arises due to the reduction of delocalized electrons [44] in the system with increasing disorder via Cr-doping. The Sr  $3d$  spectra (not shown) have been fitted with two SOD peaks Sr  $3d_{5/2}$  and Sr  $3d_{3/2}$  confirming the presence of the Sr<sup>2+</sup> state. Figure 3(b) shows the Cr  $2p$  core spectra of SRCO15. The Cr SOD peaks labeled Cr  $2p_{1/2}$  and Cr  $2p_{3/2}$  are separated by  $\Delta E_{SO}^{Cr} \sim 9.2$  eV. These doublets are further split into two peaks corresponding to the two different oxidation states as Cr<sup>3+</sup>  $3d_{2g}^3$

and Cr<sup>6+</sup>  $3d_{2g}^0$  (splitting energy  $\sim 3.68$  eV). The peak intensity ratio of Cr<sup>6+</sup> and Cr<sup>3+</sup> peaks is found to be  $\sim 2 : 1$  [Fig. 3(b)]. The overall valence state of Cr is estimated by the relation  $Cr_{x-y}^{6+} Cr_y^{3+} = Cr_x^{4+}$ . It maintains an overall 4+ oxidation state at the Ru site. For SRCO15,  $y \sim 0.045$ , suggesting one-third of Cr is in the 3+ state and two-thirds are in the 6+ oxidation state. Thus the overall charge neutrality equation for SRCO15,  $Sr^{2+} Ru_{0.85}^{4+} Cr_{0.15}^{4.5+} O_{3+\delta}^{2-}$ , where  $\delta \sim 0.04$  (calculated from the average charge valency of oxygen [46]). The B.E. values of Ru, Cr, and Sr of SRO and SRCO15 are tabulated in Table III. Figure 3(c) shows the comparative valence-band spectra of SRO and SRCO15. The peaks centered  $\sim 1.2$  eV and 6.2 eV correspond to the Ru  $4d$ /Cr  $3d$  and O  $2p$  electrons, respectively, indicating strong hybridization between Ru/Cr and oxygen [47]. The inset in Fig. 3(c) shows a zoomed-in view of the spectral region at  $\sim 1.2$  eV, which is marked as feature A (red) and B (green) ascribed as coherent (delocalized) and incoherent (localized) electrons, respectively. In SRCO15 the spectral weight of feature A near  $E_F$  is shifted to feature B, suggesting the decrement of a delocalized electron with increasing Cr-doping in SRO. Such a shift of the delocalized electron mainly arises due to electron correlation [48]. To understand the effect of electron correlation and structure distortion in the DOS with Cr-doping, we theoretically calculated the DOS. The total density of states (TDOS) for SrRuO<sub>3</sub> is calculated with  $U = 0$ ,  $U = 3.5$  eV, and with modified lattice parameters at 15% Cr-doping (with  $U = 0$ ) as shown in Fig. 3(d). The calculated TDOS shows a half-metallic state and the bands between 2.5 and  $-9$  eV energy containing Ru  $4d$ , O  $2p$  electronic contributions consistent with the earlier reported results [34,35]. The up-spin TDOS spectra resemble the experimentally obtained valence-band spectra. It is crucial to note that in both cases, with finite  $U$  and modified lattice parameter (for SRCO15), the delocalized electron near  $E_F$  is decreased and shifted towards the localized state. Thus the Cr-doping modifies the crystal structure and induces the electron correlation in the system, hence reducing the number of itinerant electrons. This localized behavior of charge carriers is further understood through the magnetic and transport properties of SRCO.

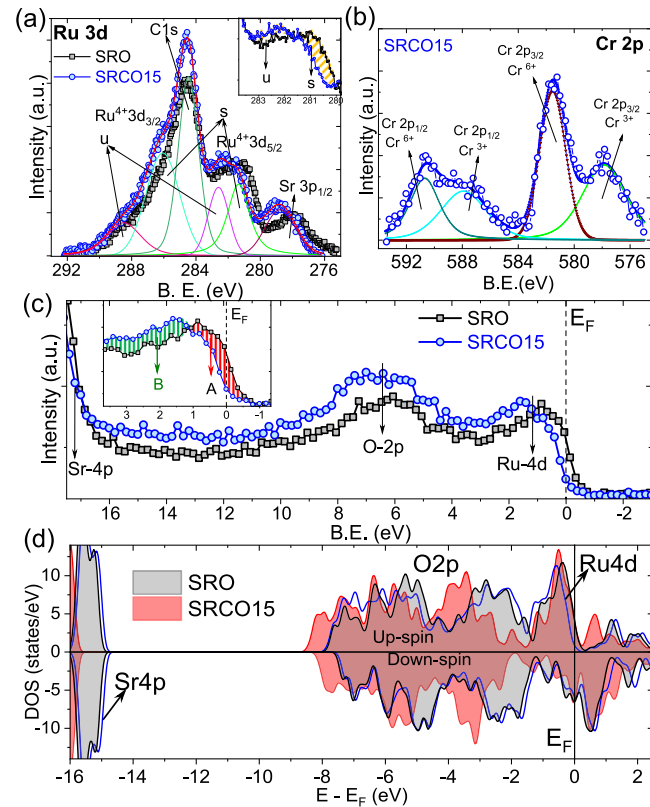


FIG. 3. Core level XPS-spectrum of (a) Ru  $3d$  in SRO and SRCO15, (b) Cr  $2p$  in SRCO15, where the open circle shows the raw data and the solid lines are the peak sum, and different colored peaks represent the fittings (using XPSPEAK-4.1 [45]). All fitting peaks are labeled according to their B.E. positions in all curves. (c) XPS valence-band spectrum of SRO and SRCO15. The insets in (a) and (c) represent the zoomed-in view of the spectra. (d) Theoretically calculated TDOS spectra for SRO with  $U = 0$  (gray),  $U = 3.5$  eV (blue-line), and SRCO15 with  $U = 0$  (red).

### C. Magnetic measurements

The structural distortion and the mixed valence state of a Cr ion certainly change the magnetic exchange interaction in SRCO. Figures 4(a) and 4(b) show the temperature-dependent FC-ZFC magnetization data of SRO and SRCO15, respectively. Both exhibit FM behavior. The FM Curie-temperature ( $T_C$ ) is calculated by fitting the FC magnetization data with the scaling law:  $M \approx (T_C - T)^\beta$ , in the vicinity of the critical region. The value of  $T_C$  turns out to be 166 and 188 K for SRO and SRCO15, respectively. The critical exponent  $\beta$  is  $\sim 0.5$  for both samples, indicating mean field type

TABLE III. The binding energy (eV) values of different constituent elements in SRO and SRCO15.

Sample	Ru $3d_{5/2}$ (eV)	Ru $3d_{3/2}$ (eV)	Sr $3p_{1/2}$ (eV)	Cr $2p_{3/2}$ (eV)	Cr $2p_{1/2}$ (eV)	Sr $3d_{5/2}$ (eV)	Sr $3d_{3/2}$ (eV)
SRO	280.75	285.95	278.0			132.21	135.21
	282.05	288.55				133.76	136.34
SRCO15	281.35	286.05	278.75	577.86 (Cr <sup>3+</sup> )	587.92 (Cr <sup>3+</sup> )	132.39	134.94
	282.6	288.5		581.54 (Cr <sup>6+</sup> )	590.69 (Cr <sup>6+</sup> )	133.64	136.34

FM-interactions. Most importantly, 22 K enhancement in the  $T_C$  is noticed, whereas the FC magnetization at 5 K ( $M_{5K}$ ) is reduced with Cr-doping (see Table IV). At low temperatures, the thermally excited magnons (following Bloch  $T^{3/2}$  law), as well as Stoner excitations (following  $T^2$  law), reduce the magnetic moment. Hence the low-temperature magnetization data fitted with  $M(H, T) = M(H, 0)[1 - A_{SW} T^{3/2} - B_{SE} T^2]$ , where  $A_{SW}$  is a spin-wave stiffness constant and  $B_{SE}$  is the Stoner excitation parameter. The value of  $A_{SW}$  is related with the exchange constant ( $J$ ) between two Ru<sup>4+</sup> atoms as  $A_{SW} = (0.0587/S)(k_B/2JS)^{3/2}$  and with  $T_C$  as  $(A_{SW})^{-2/3} = 2.42T_C$  [49]. The obtained fitting values of  $A_{SW}$  and  $B_{SE}$  decrease, and  $J$  and  $T_C$  increase with increasing Cr-doping in SRO (see Table IV). In Fig. 4(c) the exchange constant  $J \times k_B$  is plotted against the Cr-doping, which shows a gradual increase and explains the  $T_C$  enhancement.

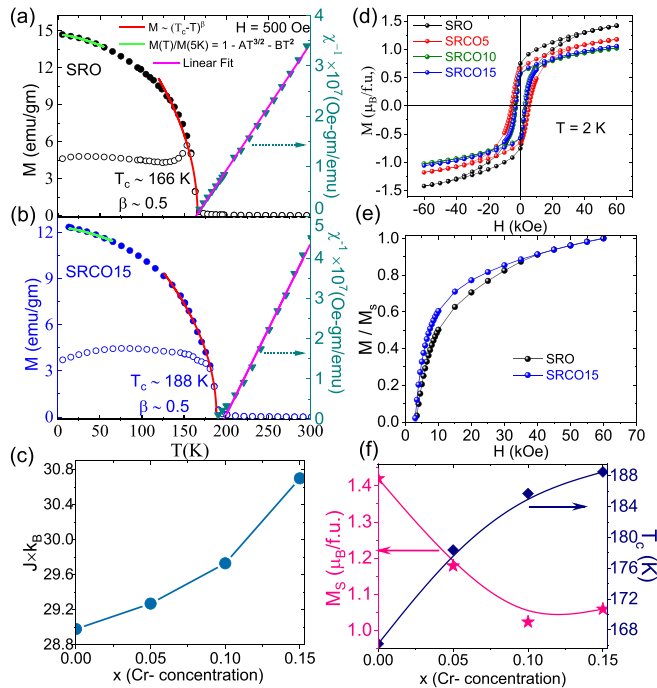


FIG. 4. Left y-axis: Temperature-dependent FC and ZFC magnetization of (a) SRO and (b) SRCO15 measured at 500 Oe, where solid red (green) lines are FC-magnetization fitting near critical region (below 50 K). Right y-axis: inverse FC-susceptibility, where pink solid lines show the Curie-Weiss linear fit. (c) Variation of  $J \times k_B$  with Cr-doping. (d)  $M - H$  hysteresis loops of SRCO samples at 2 K. (e) Comparative plot of  $M/M_s$  vs field for SRO and SRCO15. (f) Variation of  $T_C$  (right y-axis) and  $M_s$  (left y-axis) at 60 kOe with different Cr concentrations.

Figure 4(d) shows the  $M-H$  hysteresis plot at 2 K for SRCO samples. The magnetization increases up to a saturation magnetic moment with increasing magnetic field. For SRO the magnetic moment at 6 T ( $M_s$ ) is  $\sim 1.42 \mu_B/\text{f.u.}$ . This ordered moment is lower than the anticipated complete  $S = 1$  moment ( $2 \mu_B/\text{Ru}$ ), which may arise due to several reasons: (a) an itinerant ferromagnetic nature [50], (b) the spin-glass state at low temperature [16], and (c) large magnetocrystalline anisotropy (MCA). In the case of SRCO15, the resultant magnetic moment is  $\sim 25\%$  less than the parent compound SRO. In SRCO15, the origin of the reduced moment can be understood with the presence of Cr<sup>6+</sup> ( $S = 0$ ). It is important to note that the total spin-only moment is reduced (as 10% spin yields nothing). This is in agreement with the fact that an FM-like hysteresis is observed with a nonsaturating component for all SRCO samples. The nonsaturating behavior in SRO is supported by large MCA. In Cr-doped SRO, due to the randomness of exchange interactions [(a) FM with Ru<sup>4+</sup>-O-Ru<sup>4+</sup>, Ru<sup>4+</sup>-O-Cr<sup>3+</sup>, (b) PM Ru<sup>4+</sup>-O-Cr<sup>6+</sup>, and a rare possibility of (c) AFM Cr<sup>3+</sup>-O-Cr<sup>3+</sup>], a nonsaturation of the magnetization is expected. Figure 4(e) shows the comparative plot of normalized magnetization ( $M/M_s$ ) as a function of field (0–6 T). It is evident from the plot that SRO possesses a higher MCA than SRCO15. The origin of higher anisotropy in SRO compared to SRCO15 is intriguing. Below 100 K, various kinds of magnetic anomalies were observed in bulk as well as in thin-film SrRuO<sub>3</sub>. In bulk, SrRuO<sub>3</sub>, the spin glass, memory effect, slow domain-wall dynamics, anomalous magnetotransport, and Hall effect sign inversion have been observed, while in thin film exchange bias, skyrmionic behavior, topological Hall effect, etc., have been reported [17,51]. All these observations suggest the formation of a complex magnetic order below 100 K in SRO. The origin of this “complex ferromagnetism” (CFM) was found to be structural modulation driven [52]. The effect of Cr-doping reduces the anisotropy field in SRO. Such a reduction in the anisotropy field is related to the reduction of CFM in SRCO15, which is discussed in the magnetotransport section. Figure 4(f) shows the variation of  $M_s$  (at 2 K, 6 T) as well as  $T_C$  as a function of Cr-concentration. The value of  $M_s$  is decreasing with increasing Cr-doping in SRO, whereas  $T_C$  is increasing. All obtained values of  $T_C$ ,  $A_{SW}$ ,  $B_{SE}$ ,  $J$ , and  $M_{FC}$  (5 K) of SRCO15 in comparison with SRO are tabulated in Table IV. To understand the microscopic magnetism and evolution of magnetic structure, the temperature-dependent ND measurement is performed.

#### D. Neutron diffraction

Figure 5(a) shows the experimentally recorded and Rietveld-refined ND patterns for the SRCO15 sample at

TABLE IV. Magnetic parameters of SRO and SRCO15.

Parameters/ samples	$M_{5K}$ (emu/g)	$T_C$ (K)	$H_c$ (kOe)	$M_s$ ( $\mu_B$ /f.u.)	$A_{SW}$ ( $K^{-3/2}$ )	$B_{SE}$ ( $K^{-2}$ )	$J \times k_B$	$T_C^{cal}$ (K)
SRO	17.6	166.2	3.30	1.42	$1.33 \times 10^{-4}$	$2.3 \times 10^{-6}$	28.98	158.6
SRCO15	13.4	188.5	2.88	1.05	$1.22 \times 10^{-4}$	$2.04 \times 10^{-6}$	30.7	167.9

various temperatures (5–300 K). The peaks at  $Q \sim 1.6 \text{ \AA}^{-1}$  ( $2\theta = 16^\circ$ ) in the neutron diffraction data correspond to magnetic Bragg peaks (101) and (020). To get the pure magnetic signal, the nuclear background (PM-state) taken at 250 K is subtracted from the low-temperature data (below the magnetic ordered state). Figure 5(b) shows such background subtracted data for various temperatures. The intensity of the magnetic peak ( $Q \sim 1.6 \text{ \AA}^{-1}$ ) starts to appear below 190 K and attains a maximum at 5 K. This reveals a ferromagnetic ordering with a propagation vector,  $\mathbf{k} = (0,0,0)$ , as reported for the parent compound  $\text{SrRuO}_3$  [52]. To determine the symmetry of all the allowed magnetic structures of SRCO15, representation analysis [53–55] is carried out using the BASIREPS program [39]. The symmetry analysis for the space group  $Pnma$  and the propagation vector  $\mathbf{k} = (0,0,0)$  reveal four possible nonzero irreducible representations ( $\Gamma_1, \Gamma_3, \Gamma_5$ , and  $\Gamma_7$ ) (Table V). Out of these four irreducible representations, the best agreement of the experimentally observed diffraction pattern to the Rietveld refined magnetic diffraction pattern is achieved for  $\Gamma_5$ . Since the experimental value of the magnetic form factor for  $\text{Ru}^{4+}$  is not available in the literature, the magnetic form factor of  $\text{Ru}^{3+}$  is used to solve the magnetic refinement of the diffraction patterns of SRCO15 (similar to the magnetic refinement for several other  $\text{Ru}^{4+}$ -based compounds [56,57]). The magnetic structure obtained from the Rietveld analysis of the ND pattern is shown in Fig. 5(c). From the magnetic

structure, it is evident that the moments are lying predominantly along the  $b$ -axis. The components of the moments along the  $a$  and  $c$  are found to be negligible ( $< 0.1 \mu_B/\text{Ru}^{4+}$ ). The refined ordered moment value at 5 K is found to be  $M = 1.328 \pm 0.1 \mu_B/\text{Ru}^{4+}$ , which closely matches the experimental  $M_s$  value ( $\sim 1.1 \mu_B/\text{Ru}^{4+}$ ) of SRCO15. The temperature dependence of the ordered magnetic moment of SRCO15 and in comparison with SRO is shown in Fig. 5(d). The fitting of the power-law equation,  $\mu_B(T) = A(T_C - T)^\beta$ , finds  $T_C = 190 \text{ K}$  and  $\beta = 0.52$  [in close agreement with the experimental value ( $T_C = 188 \text{ K}$  and  $\beta = 0.5$ )]. From ND it is evident that the Cr-doping results in  $\sim 22 \text{ K}$  enhancement of FM ordering temperature, however the mean-field-like behavior remains the same. It should be noted that the ordered magnetic moment is considerably lower than the spin-only moment  $2 \mu_B/\text{Ru}^{4+}$ .

Now we begin with the question of what is the origin of enhancement in  $T_C$ . The answer lies within the evolution of structure parameters with temperature. The lattice parameters are obtained from the Rietveld analysis of all ND patterns. The variation of lattice parameters and the unit cell volume is plotted against temperature, as shown in Figs. 5(e)–5(h). A gradual contraction of the lattice constants and unit cell volume has been observed with the decrease in the temperature. The volume contraction below the ordering temperature can be understood as a spontaneous magnetostriction effect that arises due to the magnetic ordering of the atomic moments

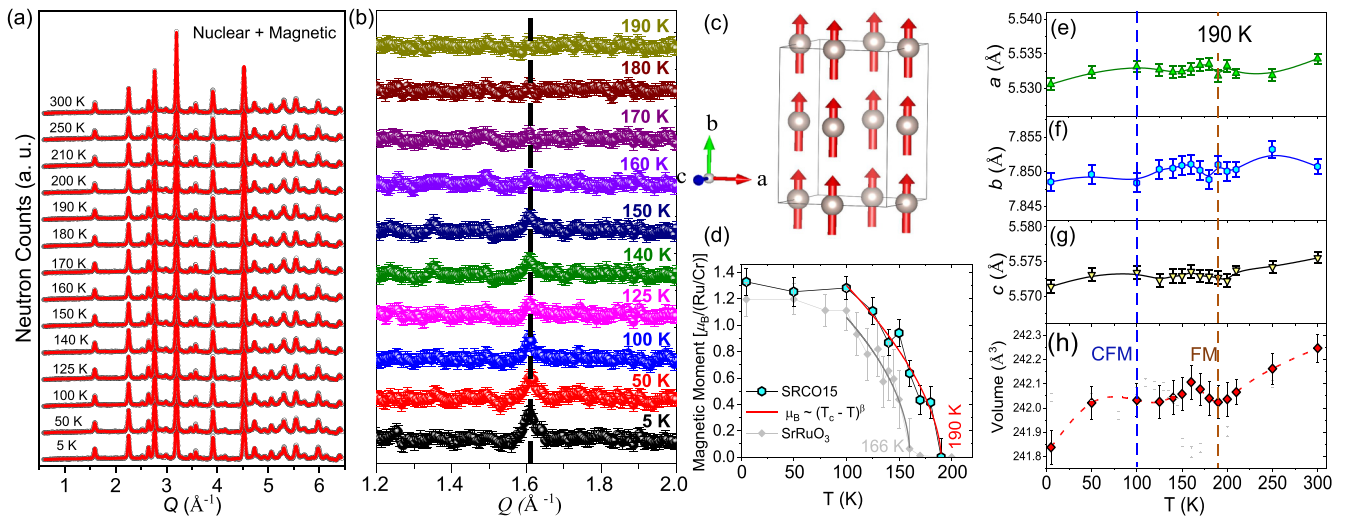


FIG. 5. (a) Neutron diffraction patterns (nuclear + magnetic) recorded over 5–300 K temperature range. (b) Temperature evolution of the magnetic Bragg peak at  $1.6 \text{ \AA}^{-1}$ . (c) The magnetic structure of SRCO15. (d) Temperature dependence of the ordered magnetic moment of SRCO15 (blue hexagon data) at the Ru site. The dashed line is the magnetic exponent fitting. Here  $\text{SrRuO}_3$  data (gray) [52] are plotted for comparison. (e)–(h) Temperature evolution of the lattice constants, and unit cell volume of SRCO15, where colored vertical dotted lines at 190 K (orange) and 100 K (blue) represent onset temperature of ferromagnetic (FM) and complex ferromagnetic (CFM) ordering, respectively.

TABLE V. Basis vectors for the atoms of the magnetic site 4b of the orthorhombic space group  $Pnma$ , with the propagation vector  $\mathbf{k} = (0,0,0)$ .

	$\psi_1(x, y, z)$	$\psi_2(-x + \frac{1}{2}, -y, z + \frac{1}{2})$	$\psi_3(-x, y + \frac{1}{2}, -z)$	$\psi_4(x + \frac{1}{2}, -y + \frac{1}{2}, -z + \frac{1}{2})$
$\Gamma_1$	(1, 1, 1)	(-1, -1, 1)	(-1, 1, -1)	(1, -1, -1)
$\Gamma_3$	(1, 1, 1)	(-1, -1, 1)	(1, -1, 1)	(-1, 1, 1)
$\Gamma_5$	(1, 1, 1)	(1, 1, -1)	(-1, 1, -1)	(-1, 1, 1)
$\Gamma_7$	(1, 1, 1)	(1, 1, -1)	(1, -1, 1)	(1, -1, -1)

below  $T_C$ . The unit cell volume resembles a minima at 190 K. A minima in unit cell volume represents a stable configuration (minimum free energy of the system), when a magnetic ordering is usually formed. Figure 6(a) shows the comparative volume plot of SRCO15 and SrRuO<sub>3</sub>. In the case of SRO, an anomaly in the lattice parameters and unit cell volume at the ferromagnetic ordering temperature (166 K). It is important to note that 0.5% volume contraction occurs only due to Cr doping, and lowering the temperature further enhances the contraction affecting the  $\Sigma$  and  $\Delta$ . Thus Cr doping results in a relative change in the crystal structure with respect to temperature. Such a change is visible in the form of a minimum in volume and a peak in  $\Delta$  near 190 K (22 K higher than the parent compound SRO). Thus the origin of the  $T_C$  enhancement is closely associated with structural modulations due to both Cr-doping and temperature. Furthermore, in the case of SrRuO<sub>3</sub>, another minimum below 100 K ( $\sim 75$  K) is noticed, which is responsible for the CFM in addition to the dominant FM order. However, Cr-doping suppresses the formation of such CFM. This picture is more clear in the transport section later. Further, the structural analysis is done from the variation of bond lengths, bond angles, and octahedral tilt. Figures 6(b) and 6(c) depict the normalized stretching and angular distortions of SRCO15 (SrRuO<sub>3</sub>), with respect to the value at 300 K (250 K), as a function of  $T/T_C$ . In the vicinity of FM ordering, the relative stretching distortion ( $\Delta/\Delta_{300K}$ ) shows a peak for both SRO and SRCO15. Such a peak in  $\Delta$  near  $T_C$  is expected. Below 100 K in SRCO15,  $\Delta$

shows an increasing trend whereas SrRuO<sub>3</sub> exhibits a peaklike feature (in the locality of CFM), while the relative angular distortion ( $\Sigma/\Sigma_{300K}$ ) shows an increasing trend down to FM ordering, and then it freezes down to  $\sim 150$  K. Lowering the temperature results in a decrease in  $\Sigma/\Sigma_{300K}$  down to 100 K and then it freezes again. Figure 6(d) displays the relative interoctahedral tilt ( $\theta/\theta_{300K}$ ) against the  $T/T_C$ . The octahedral tilt is calculated from the Ru-(O1/O2)-Ru bond angles as  $\text{tilt} = \frac{180 - \angle(\text{Ru}-(\text{O1/O2})-\text{Ru})}{2}$  [angle  $\theta$  schematically shown in Fig. 2(d)]. With lowering the temperature, the octahedral tilt along the apical plane initially increases by 2.5% and gets frozen in the vicinity of  $T_C$  followed by a reduction (while along the basal plane, it is increased) of 2.5% down to 100 K. Further lowering the temperature affects neither the apical nor basal tilt. Such freezing in the angular distortion and octahedral tilt indicates the formation of an ordered phase (in this case it is FM). To get more insight into magnetotransport, a study on various SRCO samples is carried out up to magnetic field 5 T.

### E. Transport measurements

Figure 7(a) displays the temperature-dependent normalized resistivity ( $\rho/\rho_{250K}$ ). The parent compound SRO exhibits metallic behavior down to 2 K [with a residual resistivity ratio (RRR)  $\sim 20$ ], with a slope change at  $T_C$  (166 K). A gradual increase in resistivity with Cr-doping indicates the evolution of nonmetallic behavior. Figure 7(b) depicts the variation of  $\rho_{300K}$  and  $\rho_{2K}$  with respect to Cr doping. The two and four orders of magnitude increase in the  $\rho_{300K}$  and  $\rho_{2K}$ , respectively, is estimated at 15% Cr doping in SRO. The increase in resistivity as well as the low-temperature resistivity upturn arises due to the disorder and electron correlation effect induced by Cr doping. The role of disorder and electron correlation on electrical transport can be understood by appropriate fitting of the resistivity data with various models. The parent compound shows FL to non-FL behavior  $\sim 45$  K (fitting not shown) as reported earlier [52,59]. A resistivity minima is noticed at  $T_{\min} \sim 117$  K for  $x = 0.05$ . In an itinerant electron system, such low Cr doping induces weak localization (WL) [60]. On the other hand, electron-electron interaction (EEI) in such a system also drives low-temperature resistivity upturn [61]. In correlated metals with low disorder, WL [60] and EEI [61] drive the insulating state at low temperatures. In such a case, the resistivity upturn can be fitted using the following relation [62]:

$$\rho = \frac{1}{1/\rho_0 + aT^{p/2} + bT^{1/2}} + cT^2. \quad (3)$$

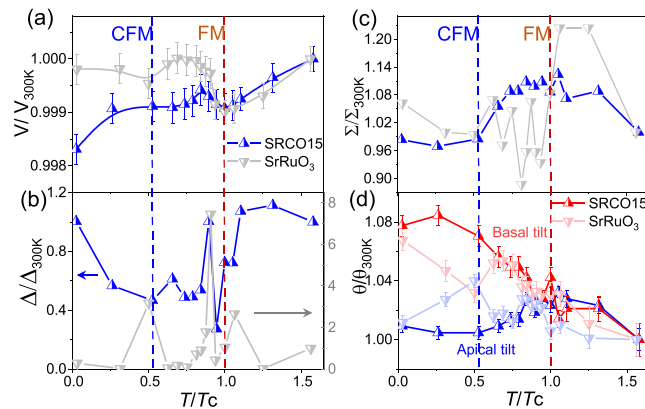


FIG. 6. The temperature variation of (a) unit cell volume and (b) stretching distortion, (c) angular distortion of Ru/CrO6 octahedra and (d) octahedral tilt angle ( $\theta$ ) for SRCO15 and SRO compounds. The values are normalized with respect to their reference values at 300 and 250 K for SRCO15 and SRO, respectively. The data for SRO are taken from [52,58].



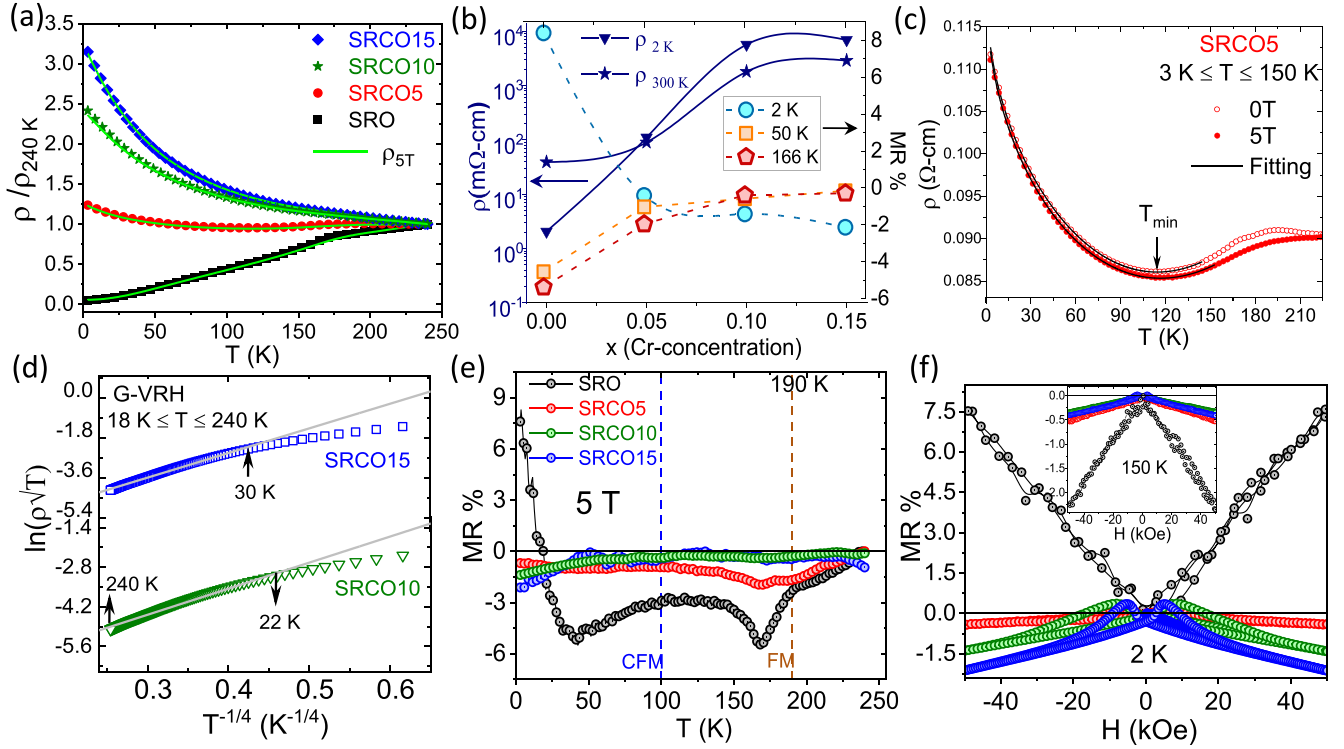


FIG. 7. (a) The temperature-dependent normalized electrical resistivity ( $\rho/\rho_{250\text{K}}$ ) of SRCO samples at 0 T (colored data points) and 5 T (solid green line). (b) Variation of  $\rho_{2\text{K}}$ ,  $\rho_{300\text{K}}$  (left y-axis), and MR% at 2, 50, and 166 K (right y-axis) with increasing Cr concentrations. (c) Resistivity fitting of SRCO5 sample with WL-model. (d) G-VRH models fitting the resistivity in SRCO10 and SRCO15. (e) MR ( $\frac{\rho(5\text{T})-\rho(0)}{\rho(0)} \times 100\%$ ) vs temperature data; vertical dotted lines represent the onset of CFM and FM. (f) MR% vs magnetic field at 2 K; inset shows MR in the vicinity of FM ordering for SRCO samples.

Here  $\rho_0$  refers to the residual resistivity, and the terms  $aT^{p/2}$  and  $bT^{1/2}$  represent WL and EEI effect, respectively. The value of  $a$  and  $b$  gives an idea about the strength of WL and EEI, respectively. In the WL term,  $p$  depends on the scattering rate of the electron's dephasing mechanism and dimensionality of the system [61]. The value of  $p$  indicates the nature of WL to be electron-electron ( $p = 2$ ) or electron-phonon ( $p = 3$ ) driven. The  $cT^2$  term in Eq. (3) represents EEI scattering at high temperatures. Figure 7(c) shows the resistivity fitting of SRCO5 using Eq. (3). The fitting parameters of resistivity at 0 and 5 T are tabulated in Table VI. The value of  $p$  turns out to be 2.98. A similar value of  $p$  has been reported for Ba- and Ti-doped SrRuO<sub>3</sub> as well [62], which indicates that the WL is mainly driven by the electron-phonon interaction. However, it is evident from the value of  $b$  ( $\sim 200a$ ; see Table VI) that EEI dominates in the overall conduction process. For  $x > 0.05$  the electron transport follows the modified Mott-variable range hopping also known as the Greaves-VRH (G-VRH) model

TABLE VI. Fitting parameters of SRCO5 resistivity at 0 and 5 T.

	$\rho_0$ ( $\Omega\text{ cm}$ )	$a$ ( $\Omega\text{ cm}^{-1}$ $\text{K}^{-p/2}$ )	$p$	$b$ ( $\Omega\text{ cm}^{-1}$ $\text{K}^{-1/2}$ )	$c$ ( $\Omega\text{ cm}$ $\text{K}^{-2}$ )
0 T	0.121	0.0015	2.98	0.32	$8.9 \times 10^{-7}$
5 T	0.119	0.0014	2.92	0.34	$7.9 \times 10^{-7}$

[63,64], where the resistivity can be expressed as

$$\rho(T) = A\sqrt{T} \exp\left[\left(\frac{T_G}{T}\right)^{1/4}\right], \quad (4)$$

where  $T_G$  is Greaves characteristic temperature and  $A$  is a prefactor. Figure 7(d) shows the G-VRH model fitting in a high-temperature regime for SRCO10 ( $T_G = 8.7 \times 10^3$  K) and SRCO15 ( $T_G = 1.7 \times 10^4$  K). The characteristic temperature  $T_G$  is inversely proportional to the localization length of a conduction electron [62,64]. With Cr-doping, the increased value of  $T_G$  indicates that the localization length of the conduction electron decreases, which suggests the system is getting localized with increasing the Cr-doping.

Furthermore, to study the magnetic contribution in transport, the magnetoresistance measurement is performed. Figure 7(e) depicts the temperature-dependent magnetoresistance ( $\text{MR}\% = \frac{\rho(H)-\rho(0)}{\rho(0)} \times 100$ ) at 5 T in SRCO. Two negative peaks in MR data are observed for the parent compound SRO. The first peak arises due to the spin fluctuation from PM to FM phase transition at  $\sim 166$  K. The second peak  $\sim 50$  K is attributed to the CFM. With small Cr-doping ( $x = 0.05$ ), the MR peak at FM order is shifted to a higher temperature ( $\sim 190$  K), and a second peak at 50 K is suppressed. However, both of these negative peaks almost disappear in the case of SRCO10 and SRCO15. Interestingly, for SRO a crossover from negative MR to positive MR is noticed near 10 K. Such a crossover in MR behavior is also reflected



from the R-H data measured at various temperatures as shown in Fig. 7(f). For SRO a large nonsaturating positive linear MR is observed at 2 K. However Cr-doped SRCO samples exhibit a negative MR. The negative MR for ferromagnetic metallic systems can be explained by using spin fluctuation theory. While the origin of positive MR in bulk SrRuO<sub>3</sub> is not known, it can be attributed to CFM in SRO. It should be noted that the 5 T field is not sufficient to align the complex magnetic structure, which can effectively increase the spin disorder scattering and hence the positive MR at low temperatures [65,66]. However, the positive MR in SrRuO<sub>3</sub> thin films has a quantum origin such as weak antilocalization due to large spin-orbit coupling, orbital effect, and Weyl fermionic nature [67–69]. The hysteretic nature in MR is observed for all SRCO samples. This hysteretic nature increases with increasing Cr doping. The value of MR is reduced to  $\sim -2\%$  for SRCO15 at 2 K as shown in Fig. 7(b) (right y-axis). At 150 K the hysteresis in MR decreases and a weak negative MR ( $\sim -0.5\%$ ) is noticed in the case of SRCO samples [inset Fig. 7(f)], whereas large negative MR ( $-2\%$ ) is observed for the parent compound (which corresponds to an FM ordering at  $\sim 166$  K). The temperature-dependent MR response of SRCO is nicely correlated with the temperature-dependent structural evolution obtained from ND data. In a nutshell, Cr doping (i) distorts the crystal structure, (ii) dilutes the total number of magnetic ions, and (iii) increases the disorder in SRO. These three facts effectively establish a nonmetallic state with reduced ferromagnetic strength. This study indicates that the structural modulation with temperature enhances the  $T_C$ .

## V. CONCLUSION

Here we observe Curie-temperature enhanced by 22 K in Cr-doped SrRuO<sub>3</sub> and install nonmetallic behavior as the

delocalized Ru 4d orbitals are replaced by localized Cr 3d. The structural analysis in SrRu<sub>1-x</sub>Cr<sub>x</sub>O<sub>3</sub> ( $0 \leq x \leq 0.15$ ) finds orthorhombic (*Pnma*) crystal structures with squeezed volume. The stretching distortions of the RuO<sub>6</sub> octahedra increase up to five times at  $x = 0.15$ . XPS core-level spectra find a mixed valance state of Cr (as Cr<sup>3+</sup> and Cr<sup>6+</sup>), and the valence-band spectra exhibit spectral weight shifting of a delocalized electron towards the localized state. The low-temperature  $M(T)$  fit indicates a larger  $J$  value for SRCO than SRO, supporting higher Curie temperature. ND refinements of SRCO15 find that the magnetic moment is aligned along the *b*-axis with  $M_s = 1.3\mu_B/\text{Ru}^{4+}$ , which closely matches with the experimental value of the bulk magnetic moment at 2 K, 6 T ( $1.1\mu_B/\text{f.u.}$ ). Temperature-dependent ND analysis reveals a structural modulation that is closely associated with the enhanced  $T_C$ . The unit cell volume minima of SRCO15 shifts by 22 K compared to SRO, which exactly mimics the  $T_C$  shift. In transport, the resistivity upturn for  $x = 0.05$  and the nonmetallic behavior for  $x > 0.05$  are fitted in terms of the disorder and localization picture. The magnetotransport data reveal a gradual suppression of spin scattering near FM as well as CFM ordering and an evolution of a nonmetallic state with Cr-doping. Thus, the itinerant-localized duality of the *d*-electron becomes crucial in deciding the fate of the electronic as well as magnetic character.

## ACKNOWLEDGMENTS

The authors acknowledge SRG SERB Grants (No. SRG-2019-001104, No. CRG-2022-005726, No. EEQ-2022-000883), India, and Initiation Grant (IITK-2019-037), IIT Kanpur, for financial support. Special thanks to S. Yonezawa (Kyoto University, Japan) for the magnetic and magnetotransport measurements.

- 
- [1] R. Valenzuela, Novel applications of ferrites, *Phys. Res. Int.* **2012**, 1 (2012).
  - [2] Z. Q. Liu, C. J. Li, W. M. Lu, X. H. Huang, Z. Huang, S. W. Zeng, X. P. Qiu, L. S. Huang, A. Annadi, J. S. Chen, J. M. D. Coey, T. Venkatesan, and Ariando, Origin of the two-dimensional electron gas at LaAlO<sub>3</sub>/SrTiO<sub>3</sub> interfaces: The role of oxygen vacancies and electronic reconstruction, *Phys. Rev. X* **3**, 021010 (2013).
  - [3] K. Salama, V. Selvamanickam, L. Gao, and K. Sun, High current density in bulk YBa<sub>2</sub>Cu<sub>3</sub>O<sub>x</sub> superconductor, *Appl. Phys. Lett.* **54**, 2352 (1989).
  - [4] J. M. Rothberg, W. Hinz, T. M. Rearick, J. Schultz, W. Mileski, M. Davey, J. H. Leamon, K. Johnson, M. J. Milgrew, M. Edwards *et al.*, An integrated semiconductor device enabling non-optical genome sequencing, *Nature (London)* **475**, 348 (2011).
  - [5] W. Witczak-Krempa, G. Chen, Y. B. Kim, and L. Balents, Correlated quantum phenomena in the strong spin-orbit regime, *Annu. Rev. Condens. Matter Phys.* **5**, 57 (2014).
  - [6] S. Nakatsuji, S.-I. Ikeda, and Y. Maeno, Ca<sub>2</sub>RuO<sub>4</sub>: New mott insulators of layered ruthenate, *J. Phys. Soc. Jpn.* **66**, 1868 (1997).
  - [7] J. Longo, P. Raccach, and J. Goodenough, Magnetic properties of SrRuO<sub>3</sub> and CaRuO<sub>3</sub>, *J. Appl. Phys.* **39**, 1327 (1968).
  - [8] T. Kiyama, K. Yoshimura, K. Kosuge, H. Michor, and A. Gerfried Hilscher, Specific heat of (Sr–Ca)RuO<sub>3</sub>, *J. Phys. Soc. Jpn.* **67**, 307 (1998).
  - [9] G. Cao, S. McCall, and J. E. Crow, Observation of itinerant ferromagnetism in layered Sr<sub>3</sub>Ru<sub>2</sub>O<sub>7</sub> single crystals, *Phys. Rev. B* **55**, R672(R) (1997).
  - [10] H. T. Dang, J. Mravlje, A. Georges, and A. J. Millis, Electronic correlations, magnetism, and Hund's rule coupling in the ruthenium perovskites SrRuO<sub>3</sub> and CaRuO<sub>3</sub>, *Phys. Rev. B* **91**, 195149 (2015).
  - [11] J. F. Annett, G. Litak, B. L. Gyorffy, and K. I. Wysokinski, Spin-orbit coupling and symmetry of the order parameter in strontium ruthenate, *Phys. Rev. B* **73**, 134501 (2006).
  - [12] M. S. Laad and E. Müller-Hartmann, Origin of the non-fermi liquid behavior of SrRuO<sub>3</sub>, *Phys. Rev. Lett.* **87**, 246402 (2001).
  - [13] L. M. Wang, H.-E. Horng, and H.-C. Yang, Anomalous magnetotransport in SrRuO<sub>3</sub> films: A crossover from fermi-liquid to non-fermi-liquid behavior, *Phys. Rev. B* **70**, 014433 (2004).

- [14] R. Palai, H. Huhtinen, J. F. Scott, and R. S. Katiyar, Observation of spin-glass-like behavior in SrRuO<sub>3</sub> epitaxial thin films, *Phys. Rev. B* **79**, 104413 (2009).
- [15] A. Kanbayasi, Magnetic properties of SrRuO<sub>3</sub> single crystal, *J. Phys. Soc. Jpn.* **41**, 1876 (1976).
- [16] S. Reich, Y. Tsabba, and G. Cao, Spin glass behavior in single crystals and sintered SrRuO<sub>3</sub>, *J. Magn. Magn. Mater.* **202**, 119 (1999).
- [17] Q. Qin, L. Liu, W. Lin, X. Shu, Q. Xie, Z. Lim, C. Li, S. He, G. M. Chow, and J. Chen, Emergence of topological hall effect in a SrRuO<sub>3</sub> single layer, *Adv. Mater.* **31**, 1807008 (2019).
- [18] J. Matsuno, N. Ogawa, K. Yasuda, F. Kagawa, W. Koshibae, N. Nagaosa, Y. Tokura, and M. Kawasaki, Interface-driven topological hall effect in SrRuO<sub>3</sub>-SrIrO<sub>3</sub> bilayer, *Sci. Adv.* **2**, e1600304 (2016).
- [19] J. Lu, L. Si, Q. Zhang, C. Tian, X. Liu, C. Song, S. Dong, J. Wang, S. Cheng, L. Qu *et al.*, Defect-engineered dzyaloshinskii–moriya interaction and electric-field-switchable topological spin texture in SrRuO<sub>3</sub>, *Adv. Mater.* **33**, 2102525 (2021).
- [20] L. Wang, Q. Feng, Y. Kim, R. Kim, K. H. Lee, S. D. Pollard, Y. J. Shin, H. Zhou, W. Peng, D. Lee *et al.*, Ferroelectrically tunable magnetic skyrmions in ultrathin oxide heterostructures, *Nat. Mater.* **17**, 1087 (2018).
- [21] M. Zhernenkov, G. Fabbris, O. Chmaissem, J. Mitchell, H. Zheng, and D. Haskel, Pressure-induced volume collapse and structural phase transitions in SrRuO<sub>3</sub>, *J. Solid State Chem.* **205**, 177 (2013).
- [22] J. Pietosa, B. Dabrowski, A. Wisniewski, R. Puzniak, R. Kiyonagi, T. Maxwell, and J. D. Jorgensen, Pressure effects on magnetic and structural properties of pure and substituted SrRuO<sub>3</sub>, *Phys. Rev. B* **77**, 104410 (2008).
- [23] B. Chakoumakos, S. Nagler, S. Misture, and H. Christen, High-temperature structural behavior of SrRuO<sub>3</sub>, *Phys. B: Condens. Matter* **241-243**, 358 (1997).
- [24] M. Shepard, S. McCall, G. Cao, and J. Crow, Thermodynamic properties of perovskite aruo 3 (a= ca, sr, and ba) single crystals, *J. Appl. Phys.* **81**, 4978 (1997).
- [25] G. Cao, F. Freibert, and J. Crow, Itinerant-to-localized electron transition in perovskite CaRu<sub>1-x</sub>Rh<sub>x</sub>O<sub>3</sub>, *J. Appl. Phys.* **81**, 3884 (1997).
- [26] T. He and R. J. Cava, Disorder-induced ferromagnetism in CaRuO<sub>3</sub>, *Phys. Rev. B* **63**, 172403 (2001).
- [27] T. Petr, K. Karel, W. Anke, and H. Jiří, On the physical properties of Sr<sub>1-x</sub>Na<sub>x</sub>RuO<sub>3</sub> (x= 0-0.19), *Solid State Sci.* **12**, 1112 (2010).
- [28] L. Pi, A. Maignan, R. Retoux, and B. Raveau, Substitution at the ru site in the itinerant ferromagnet SrRuO<sub>3</sub>, *J. Phys.: Condens. Matter* **14**, 7391 (2002).
- [29] R. Gupta and A. Pramanik, Site dilution in SrRuO<sub>3</sub>: effects on structural and magnetic properties, *J. Phys.: Condens. Matter* **29**, 115801 (2017).
- [30] Z. Han, J. Budnick, W. Hines, B. Dabrowski, S. Kolesnik, and T. Maxwell, Nuclear magnetic resonance study of the enhanced ferromagnetic ordering in polycrystalline SrRu<sub>1-x</sub>Cr<sub>x</sub>O<sub>3</sub>, *J. Phys.: Condens. Matter* **17**, 1193 (2005).
- [31] G. Cao, S. McCall, J. Bolivar, M. Shepard, F. Freibert, P. Henning, J. E. Crow, and T. Yuen, Itinerant-to-localized electron transition in CaRu<sub>1-x</sub>Sn<sub>x</sub>O<sub>3</sub> and SrRu<sub>1-x</sub>Pb<sub>x</sub>O<sub>3</sub>, *Phys. Rev. B* **54**, 15144 (1996).
- [32] B. Dabrowski, S. Kolesnik, O. Chmaissem, T. Maxwell, M. Avdeev, P. W. Barnes, and J. D. Jorgensen, Increase of ferromagnetic ordering temperature by the minority-band double-exchange interaction in SrRu<sub>1-x</sub>Cr<sub>x</sub>O<sub>3</sub>, *Phys. Rev. B* **72**, 054428 (2005).
- [33] S. Zhang, S. Tan, L. Pi, C. Zhang, and Y. Zhang, The role of Ru<sup>5+</sup> in increasing tc of Cr-doped SrRuO<sub>3</sub> system, *J. Appl. Phys.* **109**, 07E156 (2011).
- [34] H. Hadipour and M. Akhavan, Effect of electron correlation in Sr(Ca)Ru<sub>1-x</sub>Cr<sub>x</sub>O<sub>3</sub>: Density functional calculation, *J. Solid State Chem.* **183**, 1678 (2010).
- [35] L. Wang, L. Hua, and L. Chen, First-principles investigation of cr doping effects on the structural, magnetic and electronic properties in SrRuO<sub>3</sub>, *Solid State Commun.* **150**, 1069 (2010).
- [36] P. Giannozzi, O. Barone, P. Bonfanti, D. Brunato, R. Car, I. Carnimeo, C. Cavazzoni, S. De Gironcoli, P. Delugas, F. Ferrari Ruffino *et al.*, Quantum espresso toward the exascale, *J. Chem. Phys.* **152**, 154105 (2020).
- [37] J. P. Perdew, K. Burke, and M. Ernzerhof, Generalized gradient approximation made simple, *Phys. Rev. Lett.* **77**, 3865 (1996).
- [38] K. Momma and F. Izumi, Vesta: A three-dimensional visualization system for electronic and structural analysis, *J. Appl. Cryst.* **41**, 653 (2008).
- [39] C. Ritter, Neutrons not entitled to retire at the age of 60: More than ever needed to reveal magnetic structures, in *Solid State Phenomena* (Trans Tech, 2011), Vol. 170, pp. 263–269.
- [40] A. J. Williams, A. Gillies, J. P. Attfield, G. Heymann, H. Huppertz, M. J. Martinez-Lope, and J. A. Alonso, Charge transfer and antiferromagnetic insulator phase in SrRu<sub>1-x</sub>Cr<sub>x</sub>O<sub>3</sub> perovskites: Solid solutions between two itinerant electron oxides, *Phys. Rev. B* **73**, 104409 (2006).
- [41] W. Lu, W. Dong Song, K. He, J. Chai, C.-J. Sun, G.-M. Chow, and J.-S. Chen, The role of octahedral tilting in the structural phase transition and magnetic anisotropy in SrRuO<sub>3</sub> thin film, *J. Appl. Phys.* **113**, 063901 (2013).
- [42] D. J. Morgan, Resolving ruthenium: Xps studies of common ruthenium m, *Surf. Interface Anal.* **47**, 1072 (2015).
- [43] H.-D. Kim, H.-J. Noh, K. H. Kim, and S.-J. Oh, Core-level x-ray photoemission satellites in ruthenates: A new mechanism revealing the mott transition, *Phys. Rev. Lett.* **93**, 126404 (2004).
- [44] J. Brar, S. Singh, K. Kuga, P. Sharma, M. Bharath, T. Takeuchi, and R. Bindu, Lattice effects on the physical properties of half-doped perovskite ruthenates, *J. Phys.: Condens. Matter* **35**, 195402 (2023).
- [45] D.-Q. Yang and E. Sacher, Carbon 1s x-ray photoemission line shape analysis of highly oriented pyrolytic graphite: the influence of structural damage on peak asymmetry, *Langmuir* **22**, 860 (2006).
- [46] L. Wu, W. Qi, X. Ge, D. Ji, Z. Li, G. Tang, and W. Zhong, Study of the dependence of the magnetic moment of la1-x srxmno3 on the sr doping level x, *Europhys. Lett.* **120**, 27001 (2017).
- [47] K. Maiti, Role of covalency in the ground-state properties of perovskite ruthenates: A first-principles study using local spin density approximations, *Phys. Rev. B* **73**, 235110 (2006).
- [48] R. S. Singh and K. Maiti, Manifestation of screening effects and A-O covalency in the core level spectra of A site elements in the ABO<sub>3</sub> structure of Ca<sub>1-x</sub>Sr<sub>x</sub>RuO<sub>3</sub>, *Phys. Rev. B* **76**, 085102 (2007).
- [49] G. J. Snyder, Critical behavior and anisotropy in single crystal SrRuO<sub>3</sub>, [arXiv:1904.12193](https://arxiv.org/abs/1904.12193).

- [50] G. Cao, S. McCall, M. Shepard, J. E. Crow, and R. P. Guertin, Thermal, magnetic, and transport properties of single-crystal  $\text{Sr}_{1-x}\text{Ca}_x\text{RuO}_3$ , *Phys. Rev. B* **56**, 321 (1997).
- [51] H. Han, H. Zhou, C. Guillemard, M. Valvidares, A. Sharma, Y. Li, A. K. Sharma, I. Kostanovskiy, A. Ernst, and S. S. Parkin, Reversal of anomalous hall effect and octahedral tilting in  $\text{SrRuO}_3$  thin films via hydrogen spillover, *Adv. Mater.* **35**, 2207246 (2023).
- [52] C. Sow, D. Samal, P. S. Anil Kumar, A. K. Bera, and S. M. Yusuf, Structural-modulation-driven low-temperature glassy behavior in  $\text{SrRuO}_3$ , *Phys. Rev. B* **85**, 224426 (2012).
- [53] A. K. Bera, S. M. Yusuf, A. Kumar, and C. Ritter, Zigzag anti-ferromagnetic ground state with anisotropic correlation lengths in the quasi-two-dimensional honeycomb lattice compound  $\text{Na}_2\text{Co}_2\text{TeO}_6$ , *Phys. Rev. B* **95**, 094424 (2017).
- [54] A. K. Bera, S. M. Yusuf, L. Keller, F. Yokaichiya, and J. R. Stewart, Magnetism of two-dimensional honeycomb layered  $\text{Na}_2\text{Ni}_2\text{TeO}_6$  driven by intermediate Na-layer crystal structure, *Phys. Rev. B* **105**, 014410 (2022).
- [55] A. Bera, S. Yusuf, and I. Mirebeau, Effect of electron doping on the magnetic correlations in the bilayered brownmillerite compound  $\text{Ca}_{2.5-x}\text{La}_x\text{Sr}_{0.5}\text{GaMn}_2\text{O}_8$ : A neutron diffraction study, *J. Phys.: Condens. Matter* **23**, 426005 (2011).
- [56] R. Ranjan, R. Garg, A. Senyshyn, M. Hegde, H. Ehrenberg, and H. Boysen, Magneto-structural study of a cr-doped caruo3, *J. Phys.: Condens. Matter* **21**, 326001 (2009).
- [57] S. Bushmeleva, V. Y. Pomjakushin, E. Pomjakushina, D. Sheptyakov, and A. Balagurov, Evidence for the band ferromagnetism in  $\text{SrRuO}_3$  from neutron diffraction, *J. Magn. Magn. Mater.* **305**, 491 (2006).
- [58] C. Sow, D. Samal, P. Anil Kumar, A. Bera, and S. Yusuf, Freezing of the octahedral tilt near ferromagnetic transition and appearance of a glassy phase at low temperature driven by the tilt instabilities in  $\text{SrRuO}_3$ , *J. Appl. Phys.* **113**, 17E122 (2013).
- [59] P. Kostic, Y. Okada, N. C. Collins, Z. Schlesinger, J. W. Reiner, L. Klein, A. Kapitulnik, T. H. Geballe, and M. R. Beasley, Non-fermi-liquid behavior of  $\text{SrRuO}_3$ : Evidence from infrared conductivity, *Phys. Rev. Lett.* **81**, 2498 (1998).
- [60] P. A. Lee and T. Ramakrishnan, Disordered electronic systems, *Rev. Mod. Phys.* **57**, 287 (1985).
- [61] P. Dai, Y. Zhang, and M. P. Sarachik, Electrical conductivity of metallic si: B near the metal-insulator transition, *Phys. Rev. B* **45**, 3984 (1992).
- [62] B. Sarkar, B. Dalal, and S. De, Correlation among disorder, electronic and magnetic phases of  $\text{SrRuO}_3$ , *J. Phys.: Condens. Matter* **27**, 116002 (2015).
- [63] G. Greaves, Small polaron conduction in  $\text{V}_2\text{O}_5\text{P}_2\text{O}_5$  glasses, *J. Non-Cryst. Solids* **11**, 427 (1973).
- [64] J. S. Lee, Y. S. Lee, T. W. Noh, S.-J. Oh, J. Yu, S. Nakatsuji, H. Fukazawa, and Y. Maeno, Electron and orbital correlations in  $\text{Ca}_{2-x}\text{Sr}_x\text{RuO}_4$  probed by optical spectroscopy, *Phys. Rev. Lett.* **89**, 257402 (2002).
- [65] H. Nagasawa, Magnetoresistance of neodymium metal, *Phys. Lett. A* **41**, 39 (1972).
- [66] H. Yamada and S. Takada, Magnetoresistance of antiferromagnetic metals due to s-d interaction, *J. Phys. Soc. Jpn.* **34**, 51 (1973).
- [67] S. C. Gausepohl, M. Lee, K. Char, R. A. Rao, and C. B. Eom, Magnetoresistance properties of thin films of the metallic oxide ferromagnet  $\text{SrRuO}_3$ , *Phys. Rev. B* **52**, 3459 (1995).
- [68] R. Gunnarsson, Anisotropic spin-orbit interaction revealed by in-plane magnetoresistance in single-oriented  $\text{SrRuO}_3$  thin films, *Phys. Rev. B* **85**, 235409 (2012).
- [69] Q. Wang, Z. Liang, L. Wang, and J. Lu, Symmetry-controlled sign reversal and anisotropy in magnetoresistance of  $\text{SrRuO}_3$  epitaxial films, *Phys. Status Solidi RRL* **17**, 2200491 (2023).

*Correction:* A missing affiliation for the fifth and sixth authors has been inserted as the fourth affiliation, along with the corresponding indicators.